Physics in Medicine &
Biology

PAPER

Adaptive k-sparse constrained dictionary learning strategy for bioluminescence tomography reconstruction

To cite this article: Bianbian Yang *et al* 2025 *Phys. Med. Biol.* **70** 205010

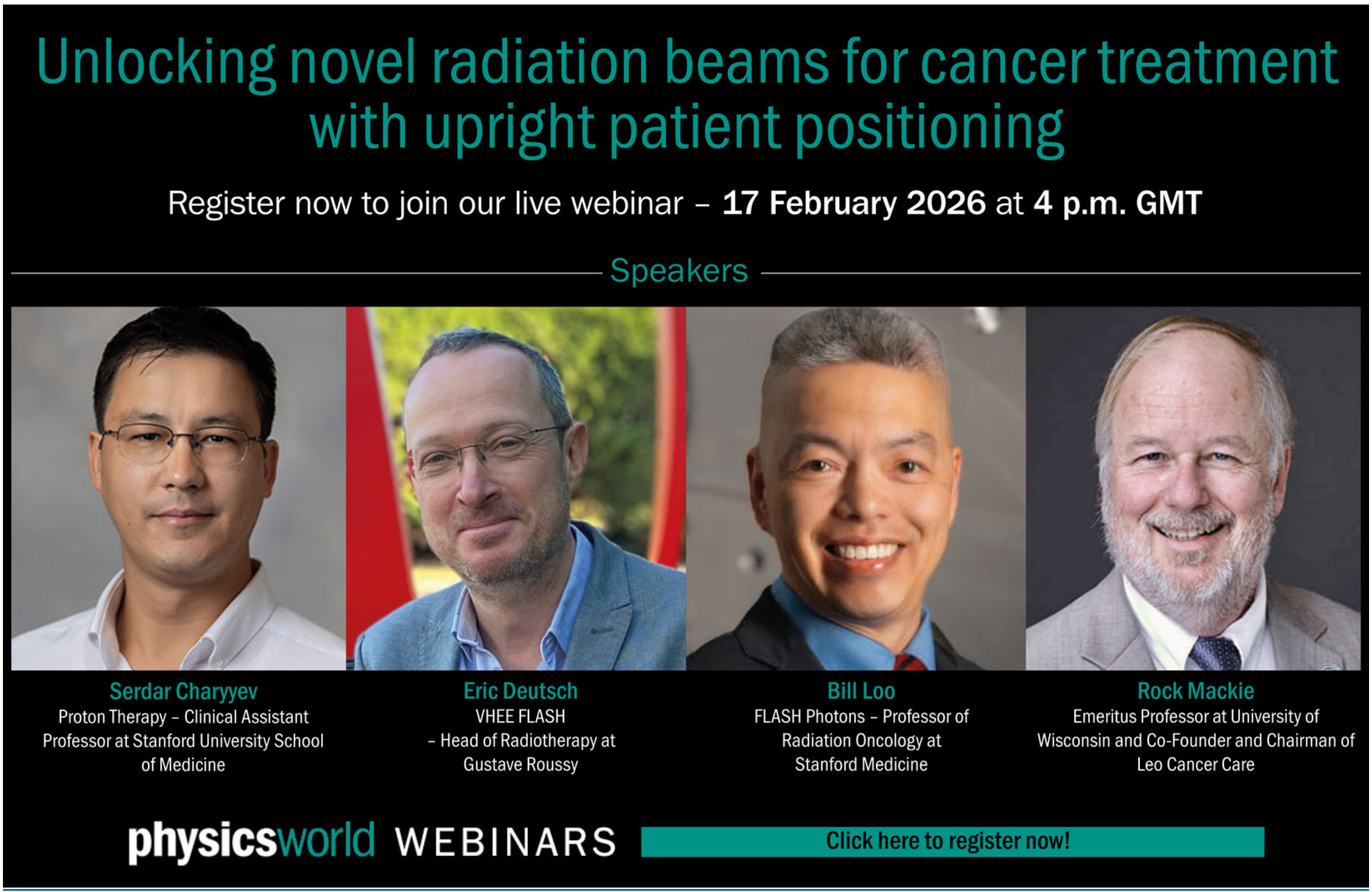

IOP Publishing Phys. Med. Biol. 70 (2025) 205010 https://doi.org/10.1088/1361-6560/ae0c51

Physics in Medicine & Biology

RECEIVED
4 July 2025

REVISED
1 September 2025

ACCEPTED FOR PUBLICATION
26 September 2025

PUBLISHED
9 October 2025

PAPER

Adaptive k-sparse constrained dictionary learning strategy for bioluminescence tomography reconstruction

Bianbian Yang[1], **Yiting He**[1], **Nannan Cai**[1], **Yi Chen**[1,2,*], **Huangjian Yi**[1], **Xingxing Hao**[1,*], **Chengyi Gao**[3] **and Xin Cao**[1,*]

[1] School of Information Science and Technology, Northwest University, Xi'an, Shaanxi 710127, People's Republic of China
[2] School of Electrical and Mechanical Engineering, The University of Adelaide, Adelaide, SA 5005, Australia
[3] Department of Oncology, The First Affiliated Hospital, Xi'an Jiaotong University, Xi'an, Shaanxi 710061, People's Republic of China
[*] Authors to whom any correspondence should be addressed.

E-mail: yichen.cgz@gmail.com, xingxing.hao@nwu.edu.cn and caoxin918@hotmail.com

Keywords: bioluminescence tomography, inverse problem, dictionary learning framework, k-sparsity strategy

Abstract

Objective. Bioluminescence tomography (BLT) is a significant molecular imaging modality with promising potential in biomedical research. However, the reconstruction results of BLT are frequently sensitive and imprecise due to the light scattering effect and ill-posed inverse problem. *Approach*. We propose an accelerated forward-backward splitting and the difference of convex functions algorithm (AFBS-DCA) based on a dictionary learning framework. In the sparse coding phase, a k-sparsity strategy enables adaptive adjustment of the regularization parameter, improving the overall efficiency. The non-convex generalized minimax-concave regularization is employed to enhance sparsity, while Nesterov's acceleration strategy improves convergence speed. During dictionary updating, DCA is utilized to efficiently solve a non-convex optimization problem modelled as a difference of two convex functions, effectively reducing computational complexity. *Main results*. The effectiveness of the AFBS-DCA method was evaluated through numerical simulations and light source implantation experiments. It achieved the highest reconstruction accuracy with an average localization error of 0.391 mm, an average Dice coefficient (DICE) of 0.774, and a contrast-to-noise ratio of 0.872. Compared with three baseline methods, the AFBS-DCA reduced reconstruction errors by 62.8%, 52.5%, and 37.8%, respectively. *Significance*. The proposed AFBS-DCA method demonstrates superior performance in terms of localization accuracy, morphological recovery, and robustness, indicating its potential to advance the practical application of BLT in biomedical research and molecular imaging.

1. Introduction

As a non-invasive and highly sensitive optical molecular imaging technique, bioluminescence imaging (BLI) has become an indispensable tool in biomedical research, especially in tracking luciferase-labelled tumours in living organisms (Guo *et al* 2017a). However, BLI can only provide two-dimensional (2D) image information, which means it cannot accurately locate the three-dimensional (3D) spatial position and morphology of the bioluminescent source in the organism, thereby limiting its in-depth application in preclinical research (Liu *et al* 2022). To overcome this limitation, bioluminescence tomography (BLT) technology has been proposed. The light propagation model and inversion algorithms are utilized in BLT to reconstruct the 3D distribution of the internal bioluminescent source based on the luminous flux measured on the surface of organisms, enabling *in vivo* visualization and quantitative analysis (Mclennan *et al* 2005, Guo *et al* 2017b).

In recent years, BLT technology has been extensively utilized in early disease diagnosis, drug development, and treatment monitoring with its superior sensitivity and non-invasive advantages, and its 3D imaging capability also provides important support for biomedical research (Qin *et al* 2012, Ren *et al* 2020). Nevertheless, BLT reconstruction remains challenging due to the intricate light scattering and absorption in biological tissues, and limited photon detection at tissue boundaries, which significantly impair reconstruction stability and accuracy (Guo *et al* 2020). Therefore, alleviating ill-posedness and improving BLT reconstruction accuracy has become a key focus in biomedical imaging research (Yang *et al* 2018).

Researchers have proposed a variety of approaches to tackle the BLT reconstruction problem, which can generally be divided into two main categories: deep learning-based methods and mathematical iteration methods (Liu *et al* 2015). Deep learning-based methods provide several advantages, including significant flexibility, high accuracy, and automated feature extraction. For example, the approach introduced by Rezaeifar *et al* shows outstanding performance in tumour targeting within BLT studies, achieving sub-millimetre tumour targeting accuracy with a median Dice similarity coefficient (DSC) of 61% in Monte Carlo simulations and a median geometrical tumour coverage of 95% with a DSC of 42% in real BLI measurements of mouse glioblastoma models (2023). However, despite these advantages, a primary challenge of deep learning-based methods is their limited interpretability, making it difficult to understand the reasoning behind their predictions. Additionally, the availability and quality of datasets remain crucial, as deep learning models heavily rely on large, high-quality datasets for effective training and generalization. This is why researchers continue to explore mathematical iterative approaches to solve the inverse problem in BLT, aiming to approximate the real bioluminescent source distribution with improved stability and accuracy, especially when combined with regularization techniques to address ill-posed problems (Kaltenbacher and Huynh 2022). Among mathematical iterative methods, regularization plays an essential role, where common loss functions include convex penalties such as the L_1-norm (Chen *et al* 2021) and L_2-norm (Cao *et al* 2007), and non-convex sparse regularization (NSR) methods. However, the L_1-norm may result in over-sparse reconstruction results, negatively impacting the accuracy of light source shape estimation, while the L_2-norm may produce over-smooth reconstructions (Zhang *et al* 2017). To overcome these limitations, various NSR methods have been proposed, such as the smoothly clipped absolute deviation method (Fan and Li 2001) and the minimax concave penalty method (Zhang 2010). The NSR approaches achieve a better balance between sparsity and accuracy compared to conventional convex regularization methods by introducing non-convexity, enabling precise sparsity control and a more flexible trade-off between sparsity and model fit (Olsson *et al* 2017).

In the research field of inverse problem solving, several iterative optimization methods have been proposed to solve objective functions, including classical approaches such as the gradient descent method and the alternating direction method of multipliers (Boyd *et al* 2010), and more advanced techniques like the fast iterative shrinkage thresholding algorithm (FISTA) (Daubechies *et al* 2010), and majorization–minimization algorithm (Lange and Yang 2000). These methods are widely applied in solving inverse optimization problems. On this basis, Bayesian approaches, as probabilistic iterative optimization methods, integrate prior knowledge into reconstruction, enhancing stability by modelling uncertainty and leveraging prior distributions (Calvetti and Somersalo 2018). For example, regularized Bayesian models such as the Gaussian Markov random field, effectively preserve target edges and improve accuracy (Feng *et al* 2009). However, their high computational complexity and reliance on intricate priors limit their flexibility. In addition to the previously discussed techniques, combining regularization with dictionary learning offers more flexible and efficient sparse representations, often outperforming Bayesian approaches (Chun and Fessler 2017). Dictionary learning involves two iterative stages: sparse coding and dictionary update. Sparse coding computes sparse representations based on a fixed dictionary, while dictionary update optimizes the dictionary for improved adaptability and accuracy (Li *et al* 2020). Typically, orthogonal matching pursuit (Wang and Shim 2012), a common sparse coding method, iteratively selects relevant dictionary atoms to approximate the signal and minimize residual error but suffers from high computational complexity, especially with large dictionaries or high-dimensional signals. Another notable approach, the k-sparse approximation and orthogonal procrustes analysis (KSAOPA) improves reconstruction stability by enforcing sparsity through k-coefficients Lipschitzian mappings while refining dictionary atoms using orthogonal Procrustes analysis (Su *et al* 2024). However, the effectiveness of KSAOPA is partially constrained by the need for manual tuning of certain crucial parameters, such as the sparsity level K, which can introduce additional time overhead and reduce overall efficiency. The proposed method effectively overcomes this limitation while preserving accuracy.

The accelerated forward-backward splitting (FBS) and the difference of convex functions algorithm (AFBS-DCA) method based on dictionary learning framework is proposed, implementing a dual-stage optimization strategy through iterative alternation between sparse coding and dictionary update phases. This method achieves high-precision reconstruction, and fast convergence, and effectively balances sparsity and shape recovery. To improve adaptive regularization, a k-sparsity strategy is introduced in the sparse coding phase, enabling the adaptive adjustment of the regularization parameter and eliminating the need for manual and sub-optimal tuning. To increase the sparsity while maintaining the convexity of the objective function, the non-convex generalized minimax-concave (GMC) regularization (Selesnick 2017) is employed within the convex AFBS framework. Additionally, Nesterov's acceleration technique is integrated to further enhance convergence speed and computational efficiency. For efficient dictionary updates, the problem is formulated as a difference of two convex functions and solved using the DCA (Gasso *et al* 2009), which offers low computational complexity and robust convergence (Le Thi *et al* 2015). By leveraging an adaptive k-sparse strategy and NSR, our approach effectively balances reconstruction accuracy and computational efficiency. To confirm its performance, we set up two different numerical simulation experiments and light source implantation experiment comparing the AFBS-DCA algorithm with three existing methods: the incomplete variables truncated conjugate gradient algorithm (IVTCG) based on L_1-norm (He *et al* 2010), the FISTA based on L_1-norm (Beck and Teboulle 2009) and the FBS algorithm (Zhang *et al* 2021).

The rest of the paper is arranged as follows. Section 2 introduces the BLT forward model, defines the inverse problem, and presents the proposed AFBS-DCA method. Section 3 describes numerical simulations and light source implantation experiments used to verify the effectiveness of the proposed algorithm. Section 4 presents the 3D visualization results of these experiments with comparative and quantitative analyses. Section 5 summarizes the main contributions of the study.

2. Methods

2.1. Traditional numerical model method for BLT reconstruction

In BLT reconstruction, the diffusion equation (DE) is commonly used to describe the process of light propagation in phantom models and experimental mice due to the high scattering and low absorption properties of biological tissues (Huang and Yu 2018). DE is a simplified approximation of the radiation transfer equation, which describes light propagation in a strictly controlled light-free environment through the first-order spherical harmonic expansion (Zhang *et al* 2011). The BLT experimental environment is a strictly controlled light-free environment, ensuring that there is no interference from any external light source (Wen *et al* 2018). Therefore, Robin boundary conditions are applied, assuming all light reaching the boundary is completely reflected and does not escape into the surroundings (Yang *et al* 2012).

The steady-state DE with Robin boundary condition is expressed as follows:

$$\begin{cases} -\nabla\cdot\left[D\left(r\right)\nabla\phi\left(r\right)\right]+\mu_a\left(r\right)\phi\left(r\right)=S\left(r\right),r\in\Omega \\ \phi\left(r\right)+2A\left(n\right)D\left(r\right)\left[\boldsymbol{v}\left(\boldsymbol{r}\right)\cdot\nabla\phi\left(r\right)\right]=0,r\in\partial\Omega \end{cases} \tag{1}$$

where S is the internal light source intensity distribution; ϕ represents luminous flux density; Ω is the domain of the organism; $\partial\Omega$ is the boundary region of the organism; $\boldsymbol{v}$ is the outward normal vector; n is the refraction coefficient of the organism. $D\left(r\right)=\frac{1}{3\left[\mu_{\mathrm{a}}+\left(1-g\right)\mu_{\mathrm{s}}\right]}$ represents the diffusion coefficient at position r, where μ_{a} and μ_{s} are the absorption and optical scattering coefficients; g is the anisotropic parameter; $A\left(n\right)$ is the refractive index mismatch factor at the interface between organism and air, as shown in equation (2):

$$A\left(n\right)=\frac{1+\left(1.4399n^{-2}+0.7099n^{-1}+0.6681+0.636n\right)}{1-\left(1.4399n^{-2}+0.7099n^{-1}+0.6681+0.636n\right)}. \tag{2}$$

According to the Robin boundary condition, the theoretical value of the light intensity density passed through the biological surface can be calculated as follows:

$$\Gamma\left(r\right)=-D\left(r\right)\left[\boldsymbol{v}\left(\boldsymbol{r}\right)\cdot\nabla\phi\left(r\right)\right]=\phi\left(r\right)/2A\left(n\right). \tag{3}$$

By applying the finite element method (FEM) to solve the photon transmission model, a crucial linear relational expression is established, which connects the luminous flux on the surface of biological tissue with the internal bioluminescent source distribution (Gasso *et al* 2009):

$$\boldsymbol{AX}=\boldsymbol{\Phi} \tag{4}$$

where $\boldsymbol{A}$ is a $m\times n$ system matrix, which contains the specific optical property information of each part of the organism. The light intensity density on the surface of the organism $\boldsymbol{\Phi}$ can be obtained by practical measurement, and it is a column vector of $m\times 1$ dimension. $\boldsymbol{X}$ is a coefficient vector with $n\times 1$ dimension.

2.2. The AFBS-DCA dictionary learning method for BLT reconstruction

BLT reconstruction is inherently ill-posed due to strong light scattering and absorption in biological tissues (Yang *et al* 2012), resulting in most photons being unable to penetrate the tissue to reach the detector. Therefore, the measurable fluorescence signal is very limited, while the number of unknowns in the source distribution far exceeds the number of observations (Ding *et al* 2014). This imbalance makes it almost impossible to obtain a unique solution by solving equation (4) directly, which brings difficulties to the accurate reconstruction of tumour localization (Hu *et al* 2012).

To alleviate the ill-posedness of the inverse problem and attain a stabilized solution, additional constraints are typically added to the BLT reconstruction process by introducing regularization into the objective function (Hu *et al* 2020). Here, the non-convex GMC regularization is employed as a penalty term to constrain equation (4), leading to the formulation of equation (5):

$$\min_{\boldsymbol{X}}\left\{F(\boldsymbol{X})=\frac{1}{2}||\boldsymbol{AX}-\boldsymbol{\Phi}||_F^2+\alpha J_{\mathrm{GMC}}(\boldsymbol{X})\right\} \tag{5}$$

where the subscript F denotes the Frobenius norm of a matrix, defined as the square root of the sum of the squared elements, that is $||\boldsymbol{A}||_F=\sqrt{\sum_{i,j}|a_{ij}|^2}$. The parameter α is the regularization coefficient controlling the sparsity level. J_{GMC} represents the sparse regularization term, which imposes a normalization constraint on the column vectors of the dictionary $\boldsymbol{A}$. GMC regularization can preserve the convexity of the objective function, reducing the risk of false local minima (Tan *et al* 2020). The GMC penalty is defined as follows:

$$J_{\mathrm{GMC}}(\boldsymbol{X})=||\boldsymbol{X}||_1-\min_{\boldsymbol{Z}}\left\{||\boldsymbol{Z}||_1+\frac{\lambda}{2\alpha}||\boldsymbol{A}(\boldsymbol{X}-\boldsymbol{Z})||_F^2\right\} \tag{6}$$

where $\boldsymbol{Z}$ is an auxiliary variable with $n\times 1$ dimension. $||\boldsymbol{X}||_1$ is the L_1-norm of the vector $\boldsymbol{X}$, which is defined as the sum of absolute values of elements for $\boldsymbol{X}$.

According to the GMC penalty, the cost function can be formulated as follows:

$$\begin{aligned}F(\boldsymbol{X})&=\frac{1}{2}||\boldsymbol{AX}-\boldsymbol{\Phi}||_F^2+\alpha||\boldsymbol{X}||_1-\min_{\boldsymbol{Z}}\left\{\alpha||\boldsymbol{Z}||_1+\frac{\lambda}{2}||\boldsymbol{A}(\boldsymbol{X}-\boldsymbol{Z})||_F^2\right\}\\&=\max_{\boldsymbol{Z}}\left\{\frac{1}{2}||\boldsymbol{AX}-\boldsymbol{\Phi}||_F^2+\alpha||\boldsymbol{X}||_1-\alpha||\boldsymbol{Z}||_1-\frac{\lambda}{2}||\boldsymbol{A}(\boldsymbol{X}-\boldsymbol{Z})||_F^2\right\}\\&=\max_{\boldsymbol{Z}}\left\{\frac{1}{2}(1-\lambda)||\boldsymbol{AX}||_F^2+\alpha||\boldsymbol{X}||_1+\varphi(\boldsymbol{X},\boldsymbol{Z})\right\}\\&=\frac{1}{2}(1-\lambda)||\boldsymbol{AX}||_F^2+\alpha||\boldsymbol{X}||_1+\max_{\boldsymbol{Z}}\{\varphi(\boldsymbol{X},\boldsymbol{Z})\}\end{aligned} \tag{7}$$

where the function $\varphi(\boldsymbol{X},\boldsymbol{Z})=\left(\frac{1}{2}||\boldsymbol{\Phi}||_F^2-\alpha||\boldsymbol{Z}||_1-\frac{\lambda}{2}||\boldsymbol{AZ}||_F^2\right)+\left\langle\boldsymbol{X},\boldsymbol{A}^T(\lambda\boldsymbol{AZ}-\boldsymbol{\Phi})\right\rangle$ is affine in $\boldsymbol{X}$ for any fixed $\boldsymbol{Z}$, and affine functions are convex (Tan *et al* 2020). Moreover, since $F(\boldsymbol{X})$ is the pointwise supremum of convex functions over $\boldsymbol{Z}$, it remains convex. This shows that the GMC regularization not only preserves the convexity of the objective function when $0<\lambda<1$, but also enhances the sparsity of the coefficient vector.

Based on the above GMC sparse regularization, we can define the following dictionary learning cost function:

$$\left(\widehat{\mathbf{X}},\widehat{\mathbf{A}},\widehat{\mathbf{Z}}\right)=\arg\min_{\mathbf{A},\mathbf{X}}\max_{\mathbf{Z}}F(\mathbf{X},\mathbf{A},\mathbf{Z}) \tag{8}$$

where $F(\boldsymbol{X},\boldsymbol{A},\boldsymbol{Z})$ is as follows:

$$F(\boldsymbol{X},\boldsymbol{A},\boldsymbol{Z})=\frac{1}{2}||\boldsymbol{AX}-\boldsymbol{\Phi}||_F^2+\alpha||\boldsymbol{X}||_1-\alpha||\boldsymbol{Z}||_1-\frac{\lambda}{2}||\boldsymbol{A}(\boldsymbol{X}-\boldsymbol{Z})||_F^2. \tag{9}$$

In this work, an alternating optimization method based on a dictionary learning framework is used to solve the dictionary matrix $\boldsymbol{A}$, the coefficient vector $\boldsymbol{X}$, and the auxiliary variable $\boldsymbol{Z}$. The AFBS-DCA algorithm is applied to iteratively perform sparse coding and dictionary updating, as detailed below.

2.2.1. Sparse coding based on AFBS algorithm

During the sparse coding phase, the GMC regularization preserves the convexity of the objective function when the parameter λ is between 0 and 1, making it solvable by the AFBS convex optimization algorithm (Wang *et al* 2018). In this algorithm, the objective coefficient vector $\boldsymbol{X}$ and auxiliary variable $\boldsymbol{Z}$ are iteratively updated with a fixed dictionary $\boldsymbol{A}$, as follows:

$$\left(\boldsymbol{X}^{(j+1)},\boldsymbol{Z}^{(j+1)}\right)=\arg\min_{\boldsymbol{X}}\max_{\boldsymbol{Z}}F(\boldsymbol{X},\boldsymbol{Z}) \tag{10}$$

$$\boldsymbol{X}^{(j+1)}=\arg\min_{\boldsymbol{X}}F(\boldsymbol{X})=\frac{1}{2}||\boldsymbol{AX}-\boldsymbol{\Phi}||_F^2+\alpha||\boldsymbol{X}||_1-\frac{\lambda}{2}||\boldsymbol{A}(\boldsymbol{X}-\boldsymbol{Z})||_F^2 \tag{11}$$

$$\boldsymbol{Z}^{(j+1)} = \underset{\boldsymbol{Z}}{\operatorname{argmin}} F(\boldsymbol{Z}) = \alpha||\boldsymbol{Z}||_1 + \frac{\lambda}{2}||\boldsymbol{A}(\boldsymbol{X}-\boldsymbol{Z})||_F^2 \tag{12}$$

where $F(\boldsymbol{X},\boldsymbol{Z})$ is a saddle-point function that exhibits convexity with respect to $\boldsymbol{X}$ and concavity with respect to $\boldsymbol{Z}$. Therefore, the proximal gradient algorithm AFBS can be utilized to achieve the global optimal solution.

In general, the AFBS algorithm is used to solve the following forms of minimization problems:

$$\min_x f_1(x) + f_2(x). \tag{13}$$

For the objective function to be solved in the sparse coding stage: $f_1(x)$ represents the data fidelity term, given by $f_1(x) = \frac{1}{2}||\boldsymbol{AX}-\boldsymbol{\Phi}||_F^2$, which ensures the reconstructed signal approximates the observed measurements. This term is convex and differentiable. $f_2(x)$ represents the L_1-norm regularization term, given by $f_2(x) = \alpha||\boldsymbol{Z}||_1$, which promotes sparsity. The function $f_2(x)$ is arbitrarily convex but not necessarily smooth.

Let $P(x) = \nabla f_1(x) = \boldsymbol{A}^{\mathrm{T}}(\boldsymbol{AX}-\boldsymbol{\Phi})$, $Q(x) = \partial f_2(x) = \alpha\operatorname{sign}(\boldsymbol{Z})$, where $\operatorname{sign}(\boldsymbol{Z})$ is the sign function, which preserves the sign of the elements in $\boldsymbol{Z}$ while applying the soft-thresholding operator. It is defined as: $\operatorname{sign}(\boldsymbol{Z}) = \begin{cases} 1, & Z>0 \\ 0, & Z=0 \\ -1, & Z<0 \end{cases}$. $P(x)$ is the gradient of the smooth objective function $f_1(x)$, while $Q(x)$ is the sub-gradient of the objective function $f_2(x)$:

$$\omega^{(j)} = x^{(j)} - \mu P\left(x^{(j)}\right) \tag{14}$$

where $\omega^{(j)}$ represents an intermediate variable obtained by a gradient descent step on $f_1(x)$, commonly used in proximal gradient methods to handle non-smooth terms (Beck and Teboulle 2009). It provides a temporary update before applying the soft-thresholding to enforce sparsity in $\boldsymbol{X}$.

The AFBS algorithm is applied to solve the L_1-norm regularization optimization, and the update rule is as follows:

$$\omega^{(j)} = \boldsymbol{X}^{(j)} - \mu\boldsymbol{A}^{\mathrm{T}}\left(\boldsymbol{AX}^{(j)} - \boldsymbol{\Phi}\right) \tag{15}$$

$$\boldsymbol{X}^{(j+1)} = \operatorname{soft}\left(\omega^{(j)},\alpha\mu\right) = \operatorname{sign}(\boldsymbol{X})\max\left(\left|\omega^{(j)}\right| - \alpha\mu, 0\right) \tag{16}$$

where $\operatorname{soft}\left(\omega^{(j)},\alpha\mu\right)$ represents the soft-thresholding operator used to promote sparsity. The thresholding parameter $\alpha\mu$ is determined by the regularization parameter α and the step size μ, controlling the extent to which values in $\omega^{(j)}$ are shrunk towards zero.

To further improve efficiency, Nesterov's acceleration technique (Phan *et al* 2018) is employed to update $\boldsymbol{X}$ and $\boldsymbol{Z}$, accelerating convergence of the algorithm. We infer $\omega^{(j+1)}$ from the current $\omega^{(j)}$ and the last iteration of $\omega^{(j-1)}$, aiming to find a better $\omega^{(j+1)}$ and $\omega^{(j)}$ to calculate $\boldsymbol{X}^{(j+1)}$:

$$\omega^{(j+1)} = (1-\tau)\,\omega^{(j)} + \tau\omega^{(j-1)} \tag{17}$$

where the parameter τ is a momentum factor in Nesterov's acceleration technique, which determines how much influence the previous iterate $\omega^{(j-1)}$ has on the current iterate $\omega^{(j+1)}$ (Phan *et al* 2018). When τ is small, the update relies mostly on the current value $\omega^{(j)}$, leading to a more conservative update; when τ is large, more weight is given to $\omega^{(j-1)}$, introducing a momentum effect that helps accelerate convergence.

The updating rules of the AFBS algorithm are as follows, where we incorporate a k-sparsity strategy for adaptively selecting the regularization parameter λ (Wang *et al* 2018):

$$\begin{cases} \omega_1^{(j)} = \boldsymbol{X}^{(j)} - \mu\boldsymbol{A}^{\mathrm{T}}\left(\boldsymbol{AX}^{(j)} - \boldsymbol{\Phi}\right) + \mu\lambda\boldsymbol{A}^{\mathrm{T}}\boldsymbol{A}\left(\boldsymbol{X}^{(j)} - \boldsymbol{Z}^{(j)}\right) \\ \omega_2^{(j)} = \boldsymbol{Z}^{(j)} + \mu\lambda\boldsymbol{A}^{\mathrm{T}}\boldsymbol{A}\left(\boldsymbol{X}^{(j)} - \boldsymbol{Z}^{(j)}\right) \\ T^{(j)} = \omega_1{}^{(j)}_{[k]} \\ \omega_1^{(j+1)} = (1-\tau)\,\omega_1^{(j)} + \tau\omega_1^{(j-1)} \\ \omega_2^{(j+1)} = (1-\tau)\,\omega_2^{(j)} + \tau\omega_2^{(j-1)} \\ \boldsymbol{X}^{(j+1)} = \operatorname{soft}\left(\omega_1^{(j+1)}; T^{(j)}\right) \\ \boldsymbol{Z}^{(j+1)} = \operatorname{soft}\left(\omega_2^{(j+1)}; T^{(j)}\right) \end{cases} \tag{18}$$

where the convergence condition is $0 < \mu < \frac{2}{\max\left(1, \frac{\lambda}{1-\lambda}\right)} ||\boldsymbol{A}||_2$ and $0 < \lambda < 1$; ${\omega_1}_{[k]}^{(j)}$ denotes the kth largest coefficient in the vector ${\omega_1}^{(j)}$; the momentum parameter is defined as $\tau = \frac{1-t^{(j)}}{t^{(j+1)}}$ with $t^{(j+1)} = \frac{1+\sqrt{\left(1+4(t^j)^2\right)}}{2}$ and $t^{(1)} = 1$. Although this choice may lead to $\tau < 0$, it is mathematically equivalent to the classical Nesterov's acceleration scheme with a positive momentum parameter $\beta^k = \frac{t^k - 1}{t^{k+1}}$ (Phan *et al* 2018).

In the traditional AFBS algorithm, the regularization parameter λ mainly controls the soft thresholding level, determining how many coefficients are set to zero during each iteration (Beck and Teboulle 2009). Under the proposed k-sparsity strategy, although λ still appears as a fixed parameter in the equations, manual adjustment of λ is no longer required. Instead, at each iteration, the threshold $T^{(j)}$ is adaptively set to the kth largest (sorted by absolute value) element in $\omega^{(j)}$, that is $T^{(j)} = \omega_{[k]}^{(j)}$ (Wang *et al* 2018). Thus, the so-called 'adaptive adjustment of λ actually refers to dynamically adjusting the effective threshold during the iterative process, based on the desired sparsity level k, rather than manually tuning λ. This adaptive thresholding strategy enables soft thresholding to retain only the k largest coefficients while setting the rest to zero, thus eliminating the need for manual adjustment of the regularization parameter and significantly improving the efficiency (Wang *et al* 2018).

During the sparse coding phase, the iteratively updated $\boldsymbol{X}$ and $\boldsymbol{Z}$ is obtained. Following this, in the dictionary update stage, the iterative update of the dictionary matrix $\boldsymbol{A}$ is carried out by fixing $\boldsymbol{X}$ and $\boldsymbol{Z}$.

2.2.2. Dictionary update based on DCA method

In the dictionary updating stage, $\boldsymbol{A}$ is updated by minimizing the cost function in equation (19), which is expressed as a difference of two convex functions (DC) programming function (Li *et al* 2020). This formulation allows the use of DCA to iteratively solve the associated convex subproblems,

$$\boldsymbol{A}^{(j+1)} = \arg\min_{\boldsymbol{A}} F(\boldsymbol{A}) = \frac{1}{2} ||\boldsymbol{AX} - \boldsymbol{\Phi}||_F^2 - \frac{\lambda}{2} ||\boldsymbol{A}(\boldsymbol{X} - \boldsymbol{Z})||_F^2. \tag{19}$$

We define the convex DC components G and H, where the function $H(\boldsymbol{A})$ is clearly defined and differentiable, as follows:

$$min\left\{F(\boldsymbol{A}) = G(\boldsymbol{A}) - H(\boldsymbol{A}) \,|\boldsymbol{A} \in \mathbb{R}^{m\times n}\right\} \tag{20}$$

$$G(\boldsymbol{A}) = \frac{1}{2} ||\boldsymbol{AX} - \boldsymbol{\Phi}||_F^2 \tag{21}$$

$$H(\boldsymbol{A}) = \frac{\lambda}{2} ||\boldsymbol{A}(\boldsymbol{X} - \boldsymbol{Z})||_F^2. \tag{22}$$

The DCA method is applied to linearize the sub-differential of the DC component $H(\boldsymbol{A})$ and optimize equation (20). In each iteration of j, the sub-differential of DC components is as follows:

$$\begin{cases} \widetilde{\boldsymbol{A}}^{(j)} = \nabla H\left(\boldsymbol{A}^{(j)}\right) = \lambda \boldsymbol{A}^{(j)} (\boldsymbol{X} - \boldsymbol{Z})(\boldsymbol{X} - \boldsymbol{Z})^{\mathrm{T}} \\ \nabla G\left(\boldsymbol{A}^{(j)}\right) = \left(\boldsymbol{A}^{(j)}\boldsymbol{X} - \boldsymbol{\Phi}\right)\boldsymbol{X}^{\mathrm{T}} \end{cases} \tag{23}$$

In $j+1$ iterations, the function $H(\boldsymbol{A})$ is linearized, and $\boldsymbol{A}^{(j+1)}$ is updated iteratively by solving the following functions:

$$\boldsymbol{A}^{(j+1)} = \underset{\boldsymbol{A}\in\mathbb{R}^{m\times n}}{\operatorname{argmin}} \left\{G(\boldsymbol{A}) - \left\langle \widetilde{\boldsymbol{A}}^{(j)}, \boldsymbol{A} \right\rangle\right\} = \underset{\boldsymbol{A}\in\mathbb{R}^{m\times n}}{\operatorname{argmin}} \left\{\frac{1}{2} ||\boldsymbol{AX} - \boldsymbol{\Phi}||_F^2 - \left\langle \widetilde{\boldsymbol{A}}^{(j)}, \boldsymbol{A} \right\rangle\right\} \tag{24}$$

where $\widetilde{\boldsymbol{A}}^{(j)}$ denotes the sub-differential of H, $\left\langle \widetilde{\boldsymbol{A}}^{(j)}, \boldsymbol{A} \right\rangle$ represents the Frobenius inner product between two matrices, which is defined as: $\left\langle \widetilde{\boldsymbol{A}}^{(j)}, \boldsymbol{A} \right\rangle = tr\left(\widetilde{\boldsymbol{A}}(j)^{\mathrm{T}}, \boldsymbol{A}\right)$, where tr represents the trace of a matrix, defined as the sum of all the elements along the main diagonal of a square matrix.

Various methods can be used to solve equation (23), but the choice of optimization strategy significantly affects the effectiveness of the dictionary update. For instance, while the gradient descent method can directly solve equation (23), it often suffers from slow convergence. As a result, we choose to reformulate equation (23) into a program of DC form and apply the DCA algorithm for optimization. In this process, the

Algorithm 1. AFBS-DCA algorithm for BLT reconstruction.

```
Input: The system matrix $\boldsymbol{A} \in \mathbb{R}^{m\times n}$, the photon measurement $\boldsymbol{\Phi} \in \mathbb{R}^{m\times 1}$, sparse level $k$.
Initialization: The parameter $\lambda$ is positive constant, maximum parameter $j_{\max}$, $j = 0$, $t^{(1)} = 1$, $err = 1e-6$,
$\boldsymbol{X}^{(0)} \in \mathbb{R}^{n\times 1}$, and $\boldsymbol{A}^{(0)} \in \mathbb{R}^{m\times n}$ with each column normalized as unit 1.
While $\left|\left|\boldsymbol{X}^{(j)} - \boldsymbol{X}^{(j-1)}\right|\right|_2 > err$ or $j < j_{\max}$ do
    Step1: Sparse coding updating rules based on Eq. (18)
    Step2: Dictionary update flow
        $\nabla H\left(\boldsymbol{A}^{(j)}\right) = \lambda \boldsymbol{A}^{(j)}\left(\boldsymbol{X}-\boldsymbol{Z}\right)\left(\boldsymbol{X}-\boldsymbol{Z}\right)^{\mathrm{T}}$
        $\nabla G\left(\boldsymbol{A}^{(j)}\right) = \left(\boldsymbol{A}^{(j)}\boldsymbol{X} - \boldsymbol{\Phi}\right)\boldsymbol{X}^{\mathrm{T}}$
        $\boldsymbol{A}_{i:}{}^{(j+1)} = \boldsymbol{A}_{i:}{}^{(j)} - \frac{\left[\nabla G\left(\boldsymbol{A}_{i:}{}^{(j)}\right) - \nabla H\left(\boldsymbol{A}_{i:}{}^{(j)}\right)\right]}{[\eta]}$
    Step3: $j = j + 1$
End while
Output: $\boldsymbol{X} = \boldsymbol{X}^{(j+1)}$
```

update of the dictionary $\boldsymbol{A}$ involves two DC decomposition. To simply the optimization problem, we optimize $\boldsymbol{A}_i$ column by column:

$$\min_{\boldsymbol{A}\in\mathbb{R}^{m\times n}} \phi\left(\boldsymbol{A}\right) := \left\{\frac{1}{2}\left|\left|\boldsymbol{A}\boldsymbol{X} - \boldsymbol{\Phi}\right|\right|_F^2 - \left\langle \widetilde{\boldsymbol{A}}^{(j)}, \boldsymbol{A}\right\rangle\right\} = \sum_{i=1}^{n}\left\{\frac{1}{2}\left|\left|\boldsymbol{\Phi}_{i:} - \boldsymbol{A}_{i:}\boldsymbol{X}\right|\right|_2^2 - \left\langle \left(\widetilde{\boldsymbol{A}}_{i:}^{(j)}\right)^{\mathrm{T}}, \left(\boldsymbol{A}_{i:}\right)^{\mathrm{T}}\right\rangle\right\}. \tag{25}$$

We decompose ϕ into two convex functions, where ϕ_1 and ϕ_2 are defined as follows:

$$\phi_1\left(\boldsymbol{A}_{i:}\right) = \frac{1}{2}\boldsymbol{A}_{i:}\mathrm{diag}\left(\eta\right)\left(\boldsymbol{A}_{i:}\right)^{\mathrm{T}} - \left\langle \left(\widetilde{\boldsymbol{A}}_{i:}^{(j)}\right)^{\mathrm{T}}, \left(\boldsymbol{A}_{i:}\right)^{\mathrm{T}}\right\rangle \tag{26}$$

$$\phi_2\left(\boldsymbol{A}_{i:}\right) = \frac{1}{2}\boldsymbol{A}_{i:}\mathrm{diag}\left(\eta\right)\left(\boldsymbol{A}_{i:}\right)^{\mathrm{T}} - \frac{1}{2}\left|\left|\boldsymbol{\Phi}_{i:} - \boldsymbol{A}_{i:}\boldsymbol{X}\right|\right|_2^2 \tag{27}$$

where $\eta = 1_{1\times n}\left|\boldsymbol{M}\right|$, where $\boldsymbol{M} = \boldsymbol{X}\boldsymbol{X}^{\mathrm{T}}$ and $1_{1\times n}$ denotes that after taking the absolute value of each element of $\boldsymbol{M}$, the diagonal elements are extracted to form a $1_{1\times n}$ row vector. $\mathrm{diag}\left(\eta\right)$ is the diagonal matrix constructed from the diagonal elements of $\boldsymbol{M}$ and used to ensure the convexity of decomposition.

Applying DCA, on the jth iteration we can calculate $\widetilde{\boldsymbol{Z}}^{(j)}$:

$$\widetilde{\boldsymbol{Z}}^{(j)} = \nabla\phi_2\left(\boldsymbol{A}_{i:}{}^{(j)}\right) = \boldsymbol{A}_{i:}{}^{(j)}\mathrm{diag}\left(\eta\right) - \left(\boldsymbol{A}_{i:}\boldsymbol{X} - \boldsymbol{\Phi}_{i:}\right)\boldsymbol{X}^{\mathrm{T}}. \tag{28}$$

On the $j+1$ iteration, $\boldsymbol{A}^{(j+1)}$ can be calculated by solving for the following convex function:

$$\boldsymbol{A}_{i:}{}^{(j+1)} = \underset{\boldsymbol{A}_{i:}\in\mathbb{R}^{m\times n}}{\mathrm{argmin}}\left\{\phi_1\left(\boldsymbol{A}_{i:}\right) - \left\langle \widetilde{\boldsymbol{Z}}(j)^{\mathrm{T}}, \boldsymbol{A}_{i:}{}^{\mathrm{T}}\right\rangle\right\} = \left\{\boldsymbol{A}_{i:}{}^{(j)} - \frac{\left[\nabla G\left(\boldsymbol{A}_{i:}{}^{(j)}\right) - \nabla H\left(\boldsymbol{A}_{i:}{}^{(j)}\right)\right]}{[\eta]}\right\}. \tag{29}$$

Finally, the columns of the dictionary matrix $\boldsymbol{A}$ are normalized with L_2-norm to maintain numerical stability and scale consistency.

The AFBS-DCA algorithm with k-sparsity strategy is outlined in Algorithm 1.

3. Experiment design

In this section, numerical simulations and light source implantation experiment were conducted to evaluate the proposed method. Three traditional algorithms: IVTCG based on L_1-norm, FISTA based on L_1-norm, and FBS were used for comparison in terms of morphological recovery, localization accuracy, and robustness. All experiments and procedures were conducted on an AMD Ryzen 7 3700 U laptop with Radeon Vega Mobile Gfx (2.30 GHz) and 8GB of RAM.

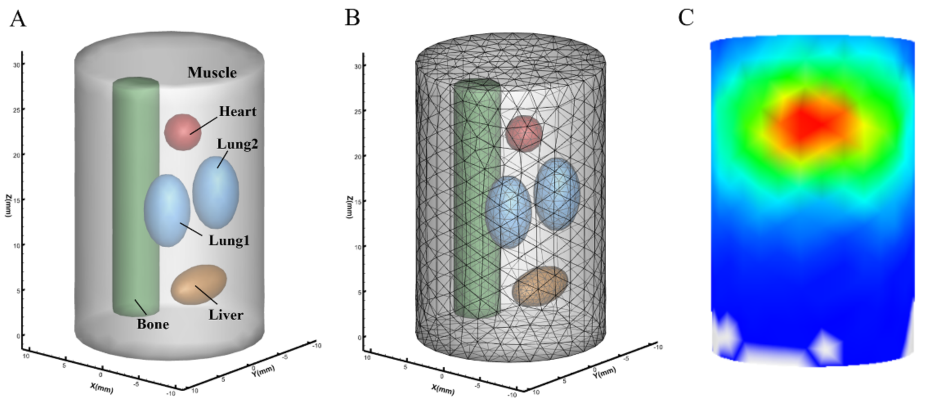

Figure 1. (A) The 3D view of the main organs of cylindrical phantom. (B) The 3D view of meshed cylindrical phantom. (C) The forward simulation result of single-source.

Table 1. Optical properties of the heterogeneous cylindrical phantom at 650 nm.

Tissues	$\mu_a(r)$ (mm^{-1})	$\mu_s(r)$ (mm^{-1})	g
Muscle	0.0052	10.80	0.900
Bone	0.0060	60.09	0.900
Heart	0.0083	6.733	0.850
Liver	0.0329	7.000	0.900
Lung	0.0133	19.70	0.900

3.1. Numerical simulation experiments setup

A non-uniform cylindrical model with a height of 30 mm and a radius of 10 mm was constructed to simulate biological structure, including five major organs: heart, bone, liver, lung, and muscle, as shown in figure 1(A). At a wavelength of 650 nm, the optical parameters of each organ are listed in table 1 (Zhang *et al* 2024).

The model was discretized using COMSOL Multiphysics 5.6 (COMSOL, Inc., Burlington, Massachusetts) software (Parvitte *et al* 2013) into 4626 nodes and 25 840 tetrahedral elements, as shown in figure 1(B). The forward simulation result of single-source was simulated with the Monte Carlo method using the molecular optical simulation environment (Ren *et al* 2010), as shown in figure 1(C).

Three experiments were designed: a single-source simulation with a 1 mm radius source cantered at (−1, −4, 22) mm; a dual-source simulation with two identical sources at (−2, −7, 10) mm and (−2, −7, 17) mm; and an anti-noise experiment where Gaussian noise of 5%, 10%, 15%, 20%, and 25% was added to the single-source simulation to evaluate the noise robustness of the AFBS-DCA method.

3.2. Light source implantation experiment setup

To verify the feasibility of the AFBS-DCA method *in vivo*, a light source implantation experiment was performed on an adult BALB/c mouse using a BLT/CT dual-mode imaging system. All experimental procedures were approved by the Animal Ethics Committee of Northwest University, China. The mouse was anesthetized with a 3% isoflurane-air mixture throughout the operation and fixed on a rotation stage to minimize motion.

A flexible plastic tube with a 1 mm radius and a 2 mm height was implanted at (6, 12, 20) mm to simulate an early tumour. Bioluminescent images were captured by an electron multiplying charge-coupled device camera (iXon Ultra 888) equipped with a 630 nm band-pass filter, with an exposure time of 1 s and no gain applied. CT imaging was performed using the CT system built into the BLT/CT device, with a tube voltage of 50 kVp and x-ray power of 40 W. The structure diagram of the dual-mode system is shown in figure 2.

After image acquisition, a landmark-based rigid registration method was applied to align bioluminescence and CT images. The 2D irradiance distribution was then projected onto the 3D surface of the mouse model. Magor organs including muscle, heart, lung, liver, stomach, and kidneys were segmented using Amira software. For reconstruction, the mouse model was meshed into 6848 nodes and 38 468 tetrahedral elements, as shown in figure 3.

3.3. Evaluation index

To further quantify the performance of different methods, three evaluation metrics were used: Localization error (LE) (Guo *et al* 2020), Dice coefficient, and the contrast to noise ratio (CNR) (Guo *et al* 2020).

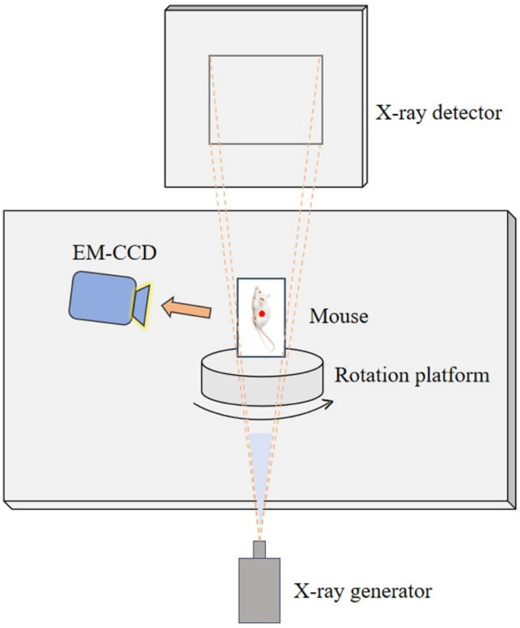

Figure 2. The device structure diagram of the BLT/CT system.

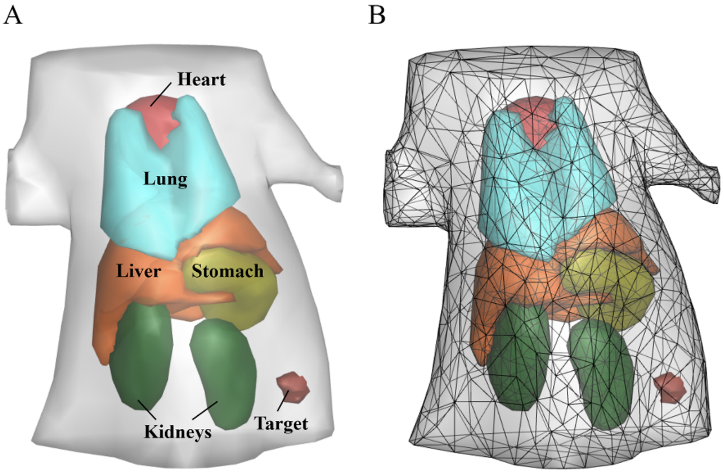

Figure 3. (A) Three-dimensional mouse model with a target. (B) Mouse tetrahedral mesh model with a target.

LE assesses spatial positioning accuracy by calculating the Euclidean distance between the reconstructed object centre (x_r, y_r, z_r) and the actual object centre (x_t, y_t, z_t). A smaller LE indicates higher positioning accuracy:

$$\mathrm{LE} = ||L_\mathrm{r} - L_\mathrm{t}||_2 = \sqrt{(x_\mathrm{r} - x_\mathrm{t})^2 + (y_\mathrm{r} - y_\mathrm{t})^2 + (z_\mathrm{r} - z_\mathrm{t})^2} \tag{30}$$

where L_r and L_t represent the centres of the reconstructed and true sources, respectively. A smaller LE indicates higher positional accuracy.

DICE evaluates morphological recovery between the reconstructed target region R_r and the real target region R_t:

$$\mathrm{DICE} = 2\frac{|R_\mathrm{r} \cap R_\mathrm{t}|}{|R_\mathrm{r}| + |R_\mathrm{t}|}. \tag{31}$$

The DICE value ranges from 0 to 1, a higher value indicates greater overlap between the reconstructed and actual target regions, reflecting better ability of morphological recovery.

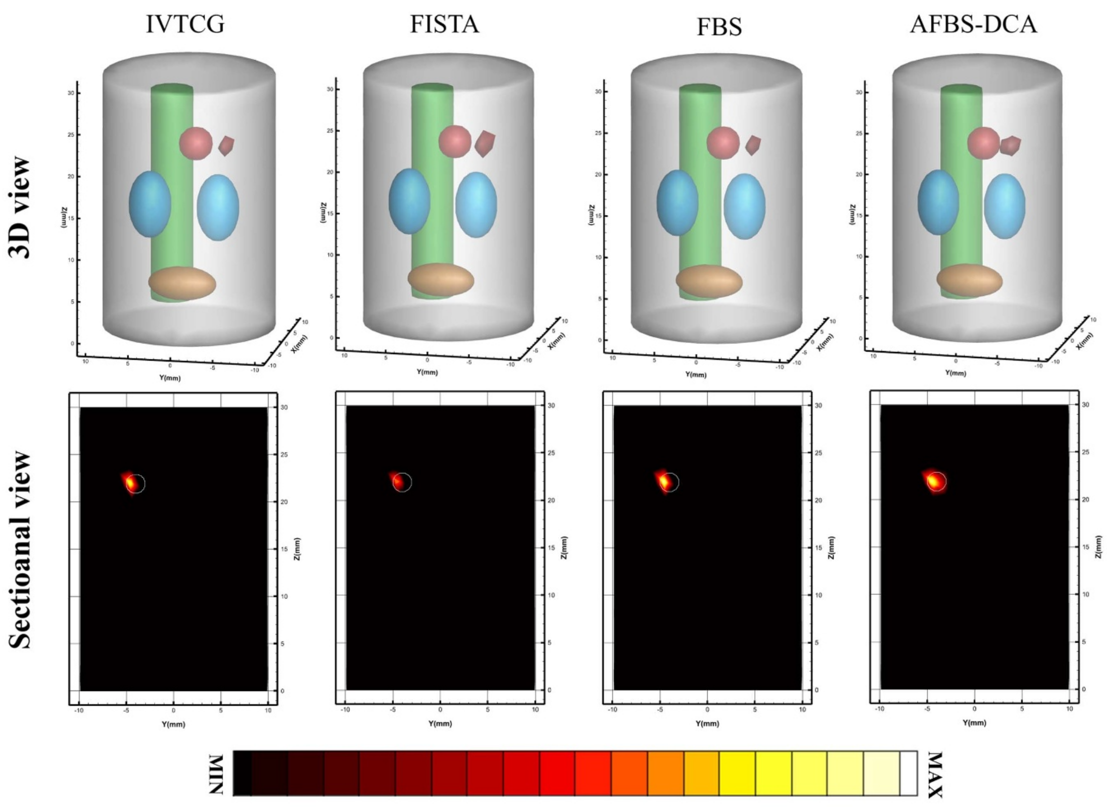

Figure 4. Comparison results of four algorithms in single-source numerical simulation experiment (3D view and sectional view).

Table 2. Quantitative results of single-source numerical simulation.

Method	Reconstructed results (mm)	LE (mm)	DICE	CNR
IVTCG-L_1	(− 1.425, − 4.536, 21.941)	0.687	0.675	0.165
FISTA-L_1	(− 1.417, − 4.629, 21.968)	0.756	0.381	0.143
FBS	(− 1.444, − 4.321, 21.879)	0.562	0.543	0.290
AFBS-DCA	(− 1.278, − 3.999, 21.976)	0.280	0.864	1.343

CNR is utilized to assess the quality of reconstruction results:

$$\mathrm{CNR} = \frac{|\mu_{\mathrm{ROI}} - \mu_{\mathrm{BCK}}|}{(m_{\mathrm{ROI}}\sigma^2_{\mathrm{ROI}} + m_{\mathrm{BCK}}\sigma^2_{\mathrm{BCK}})^{1/2}} \tag{32}$$

where μ_{ROI} and μ_{BCK} represent the mean values in the region of interest (ROI) and background, respectively; σ^2_{ROI} and σ^2_{BCK} are represent the variances; m_{ROI} and m_{BCK} represent the number of nodes included in the ROI and background, respectively. A higher CNR value indicates better reconstruction quality.

4. Results

4.1. Numerical simulations results

4.1.1. Single-source experiment

The reconstruction results of the single-source experiment are shown in figure 4. The first row displays the 3D reconstruction results of IVTCG, FISTA, FBS, and AFBS-DCA, where the reconstructed light source is depicted in red. The second row shows the cross-sectional view at the $X = -1$ mm plane, with the red area indicating the reconstructed source and the white circle denoting the actual location and boundary of the true source. In addition, the quantitative evaluation results of the four methods are summarized in table 2. It can be seen that the AFBS-DCA method achieves the lowest LE (0.280 mm), the highest DICE (0.864), and the highest CNR (1.343), indicating better positional accuracy, morphological recovery, and image contrast compared to the other methods.

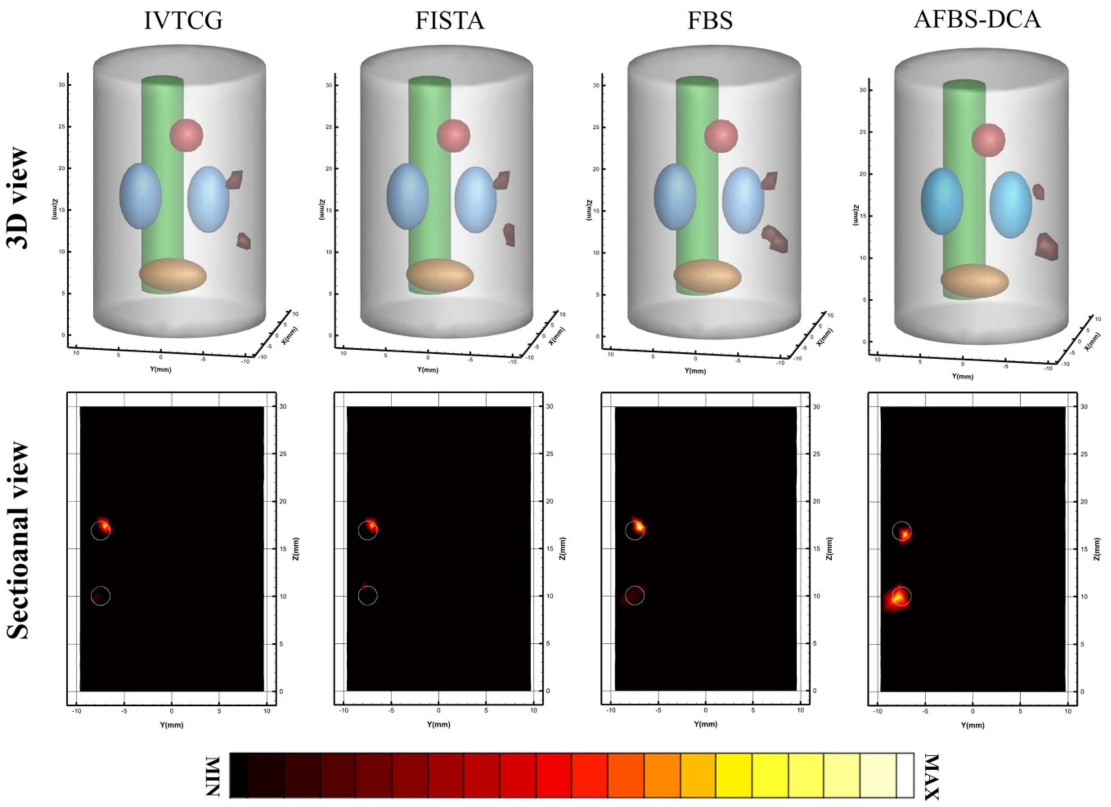

Figure 5. Comparison results of four algorithms in dual-source numerical simulation experiment (3D view and sectional view).

Table 3. Quantitative results of dual-source numerical simulation.

Method	Reconstructed results (mm)	LE (mm)	Total LE (mm)	DICE	CNR
IVTCG-L_1	(− 2.521, − 7.519, 10.445) (− 2.818, − 7.211, 17.496)	0.859 0.979	1.838	0.391 0.192	0.351
FISTA-L_1	(− 2.669, − 7.482, 10.585) (− 2.716, − 7.210, 17.475)	1.011 0.885	1.896	0.333 0.183	0.293
FBS	(− 2.225, − 7.215, 10.572) (− 2.596, − 7.151, 17.456)	0.651 0.765	1.416	0.452 0.266	0.357
AFBS-DCA	(− 1.709, − 7.180, 10.149) (− 2.335, − 7.105, 16.597)	0.373 0.505	0.878	0.744 0.769	1.148

4.1.2. Dual-source experiment

The reconstruction results of the dual-source experiment are shown in figure 5. The first row presents the 3D reconstruction results of IVTCG, FISTA, FBS, and AFBS-DCA, and the second row displays the axial view at the $X = -2$ mm plane. The reconstructed sources are shown in red, and the actual sources are marked with white circles, consistent with the single-source experiment. As summarized in table 3, the AFBS-DCA method achieves the lowest average LE (0.439 mm), reducing the reconstruction error by 54%, 52%, and 38% compared with the other methods. It also attains the highest average DICE (0.756) and CNR (1.148), indicating better positional accuracy, morphological recovery, and image contrast in dual-source reconstruction.

4.1.3. Anti-noise experiment

The results of the anti-noise experiment are shown in figure 6. Based on the single-source experiment, Gaussian noise at levels of 5%, 10%, 15%, 20%, and 25% was added to the measurement data (Liu *et al* 2022). It can be observed that the LE, DICE, and CNR values of the AFBS-DCA method show only slight

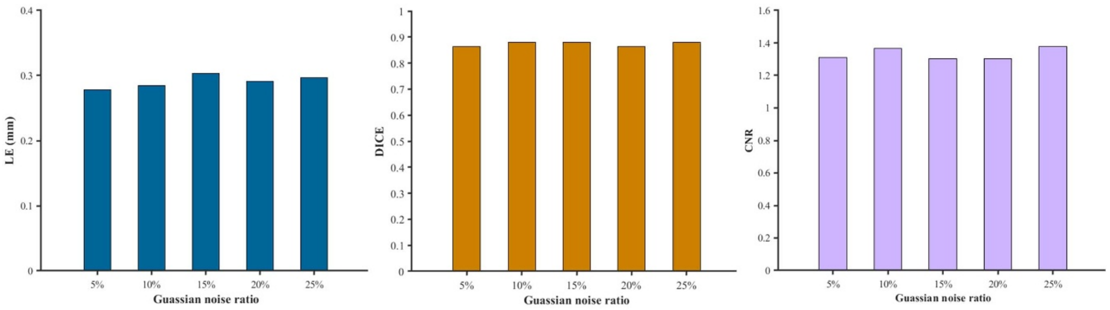

Figure 6. Anti-noise experiment result graph (LE, DICE, and CNR index).

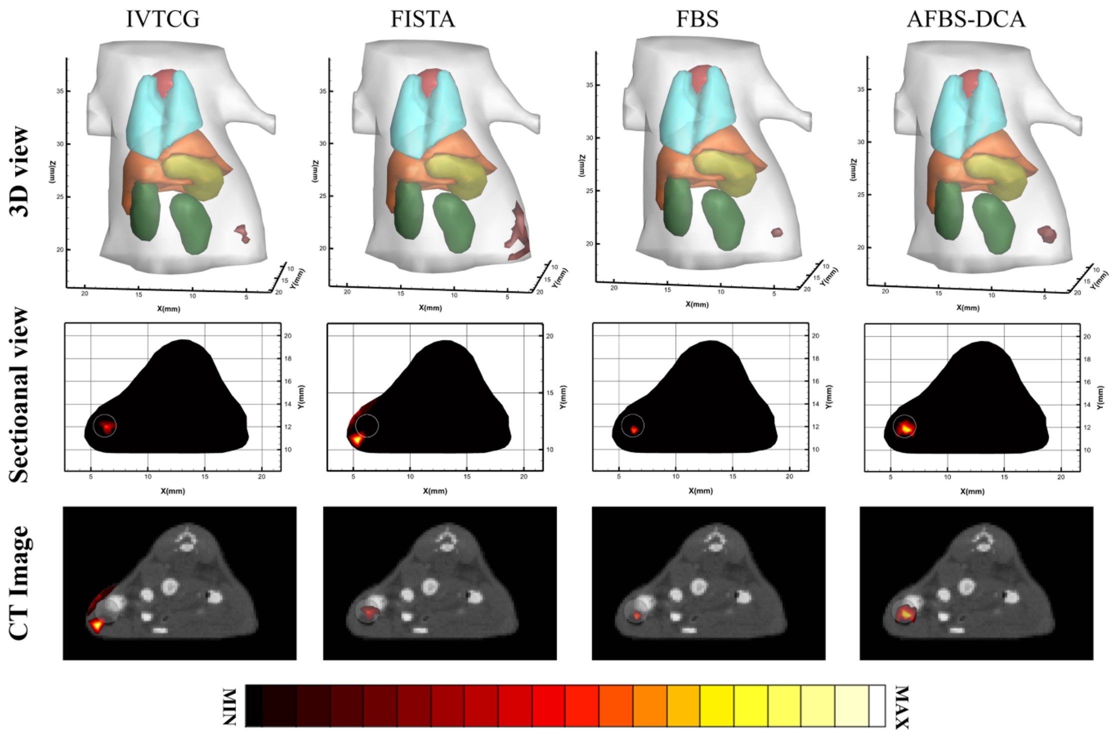

Figure 7. Comparison results of four algorithms in light source implantation experiment (3D view, sectional view and CT image).

fluctuations with increasing noise levels, indicating that the method is robust and maintains good reconstruction performance under varying noise interference.

4.2. Light source implantation experiment results

The results of the light source implantation experiment are shown in figure 7. The first to fourth columns display the 3D views, axial slices (at the plane $Z = 20$ mm), and CT-fused images reconstructed by the IVTCG, FISTA, FBS, and AFBS-DCA methods, respectively. The reconstructed light source is marked in red, and the white circular area in the slice indicates the actual source location, while the CT image provides anatomical reference. For quantitative analysis, LE, DICE, and CNR values are summarized in table 4. The AFBS-DCA method achieves the lowest LE (0.404 mm), and the highest DICE and CNR values among all methods, indicating better spatial localization, morphological recovery, and image contrast. These results confirm the effectiveness and practical applicability of AFBS-DCA in light source implantation experiment.

Table 4. Quantitative results of light source implantation experiment.

Method	Reconstructed results (mm)	LE (mm)	DICE	CNR
IVTCG-L_1	(6.736, 12.047, 20.201)	0.765	0.362	0.070
FISTA-L_1	(4.896, 11.207, 19.237)	1.558	0.138	0.001
FBS	(6.316, 11.698, 19.694)	0.533	0.140	0.036
AFBS-DCA	(6.341, 11.846, 19.845)	0.404	0.717	0.124

5. Discussion and conclusion

BLT is an advanced and non-invasive imaging modality with high sensitivity, offering significant potential for preclinical molecular imaging. However, the BLT reconstruction problem is severely ill-posed, making it highly sensitive to noise and measurement errors, resulting in instability and inaccuracy in the reconstructed bioluminescent source distribution. Traditional algorithms often suffer from slow convergence and sub-optimal solutions, while dictionary learning-based methods further increase computational complexity due to high-dimensional properties.

To address these challenges, this study proposed the AFBS-DCA method, which integrates dictionary learning with non-convex optimization strategies. In the sparse coding stage, non-convex GMC regularization is introduced to enhance sparsity, and Nesterov's acceleration technique is employed to improve convergence speed. Additionally, a k-sparsity strategy is utilized to adaptively adjust the regularization parameter, reducing the need for manual tuning. In the dictionary update stage, the DCA decomposes the original non-convex problem into a sequence of convex subproblems, thereby improving computational efficiency and feasibility.

The performance of the AFBS-DCA method was systematically evaluated through numerical simulations and light source implantation experiments, and compared with three representative methods: IVTCG-L_1, FISTA-L_1, and FBS. Experimental results consistently demonstrated that AFBS-DCA outperformed the baseline methods in terms of localization accuracy, morphological recovery, and robustness to noise. In both single- and dual-source simulations, the proposed method achieved superior reconstruction precision. Its stability under different noise levels was verified by the anti-noise experiment, while the light source implantation experiment validated its practical applicability. Quantitatively, AFBS-DCA attained an average minimum LE of 0.391 mm, an average DICE of 0.774, and an average CNR of 0.872. These results highlight the efficacy and robustness of AFBS-DCA for accurate bioluminescence source reconstruction.

Despite the superior performance demonstrated by the AFBS-DCA method, certain limitations remain, including the need to extend its applicability to other optical molecular imaging modalities and to further validate its reliability in complex biological and clinical settings. Future work will focus on broadening the method's application scope and conducting comprehensive *in vivo* and clinical studies to fully establish its practical value.

In conclusion, we proposed an AFBS-DCA method to improve the reconstruction performance of BLT. This method integrates non-convex GMC regularization to enhance sparsity, Nesterov-accelerated sparse coding for efficient convergence, and an adaptive k-sparsity strategy to reduce manual parameter tuning. In addition, a DCA-based dictionary learning framework is employed to ensure effective dictionary update and optimization. Compared with several conventional methods, AFBS-DCA demonstrates superior performance in terms of localization accuracy, morphological recovery, and robustness across both numerical simulations and light source implantation experiments. We believe that this method will provide broader application prospects and greater practical value in both preclinical and clinical biomedical research.

Data availability statement

The data cannot be made publicly available upon publication because they contain commercially sensitive information. The data that support the findings of this study are available upon reasonable request from the authors.

Acknowledgments

This work was supported in part by the National Major Scientific Research Instrument Development Projects of China (82127805), in part by the Key Research and Development Program of Shaanxi Province (2024SF-YBXM-681), in part by the National Natural Science Foundation of China (61701403, 61806164).

ORCID iD

Xin Cao 0000-0003-3560-6523

References

Beck A and Teboulle M 2009 A fast iterative shrinkage-thresholding algorithm for linear inverse problems *SIAM J. Imaging Sci.* **2** 183–202

Boyd S, Parikh N, Chu E, Peleato B and Eckstein J 2010 Distributed optimization and statistical learning via the alternating direction method of multipliers *Found. Trend Mach. Learn.* **3** 1–122

Calvetti D and Somersalo E 2018 Inverse problems: from regularization to Bayesian inference *Wiley Interdiscip. Rev. Comput. Stat.* **10** e1427

Cao N, Nehorai A and Jacobs M 2007 Image reconstruction for diffuse optical tomography using sparsity regularization and expectation-maximization algorithm *Opt. Express* **15** 13695

Chen H *et al* 2021 Smart self-assembly amphiphilic cyclopeptide-dye for near-infrared window-ii imaging *Adv. Mater.* **33** e2006902

Chun I Y and Fessler J A 2017 Convolutional dictionary learning: acceleration and convergence *IEEE Trans. Image Processing* P 1

Daubechies I, Defrise M and De Mol C 2010 An iterative thresholding algorithm for linear inverse problems with a sparsity constraint *Commun. Pure Appl. Math.* **57** 1413–57

Ding X, Wang K, Jie B, Luo Y, Hu Z and Tian J 2014 Probability method for Cerenkov luminescence tomography based on conformance error minimization *Biomed. Opt. Express* **5** 2091

Fan J and Li R 2001 Variable selection via nonconcave penalized likelihood and its oracle properties *Publ. Am. Stat. Assoc.* **96** 1348–60

Feng J, Jia K, Qin C, Yan G, Zhu S, Zhang X, Liu J and Tian J 2009 Three-dimensional bioluminescence tomography based on Bayesian approach *Opt. Express* **17** 16834–48

Gasso G, Rakotomamonjy A and Canu S 2009 Recovering sparse signals with a certain family of non-convex penalties and DC programming *IEEE Trans. Signal Process.* **57** 4686–98

Guo H, Gao L, Yu J, He X and Yang X 2020 Sparse-graph manifold learning method for bioluminescence tomography *J. Biophotonics* **13** e201960218

Guo H, Hu Z, He X, Zhang X, Liu M, Zhang Z, Shi X, Zheng S and Tian J 2017a Non-convex sparse regularization approach framework for high multiple-source resolution in Cerenkov luminescence tomography *Opt. Express* **25** 28068

Guo H, Yu J, Hu Z, Yi H, Hou Y and He X 2017b A hybrid clustering algorithm for multiple-source resolving in bioluminescence tomography *J. Biophotonics* **11** e201700056

He X, Liang J, Wang X, Yu J, Qu X, Wang X, Hou Y, Chen D, Liu F and Tian J 2010 Sparse reconstruction for quantitative bioluminescence tomography based on the incomplete variables truncated conjugate gradient method *Opt. Express* **18** 24825–41

Hu Z, Chen X, Liang J, Qu X, Chen D, Yang W, Wang J, Cao F and Tian J 2012 Single photon emission computed tomography-guided Cerenkov luminescence tomography *J. Appl. Phys.* **112** 227

Hu Z, Fang C, Li B, Zhang Z and Tian J 2020 First-in-human liver-tumour surgery guided by multispectral fluorescence imaging in the visible and near-infrared-I/II windows *Nat. Biomed. Eng.* **4** 1–13

Huang J and Yu J 2018 Bioluminescence tomography based on multilevel adaptive finite element method *Chin. J. Lasers* **45** 0607003

Kaltenbacher B and Huynh K 2022 Iterative regularization for constrained minimization formulations of nonlinear inverse problems *Comput. Optim. Appl.* **81** 569–611

Lange K and Yang H I 2000 Optimization transfer using surrogate objective functions *J. Comput. Graph. Stat.* **9** 1–20

Le Thi H, Pham Dinh T, Le H and Vo X 2015 DC approximation approaches for sparse optimization *Eur. J. Oper. Res.* **244** 26–46

Li Z, Wan C, Tan B, Yang Z and Xie S 2020 A fast dc-based dictionary learning algorithm with the SCAD penalty *Neurocomputing* **429** 89–100

Liu H, Yang X, Song T, Bao C, Shi L, Hu Z, Wang K and Tian J 2015 Multispectral hybrid Cerenkov luminescence tomography based on the finite element SPn method *J. Biomed. Opt.* **20** 086007

Liu Y, Chu M, Guo H, Hu X, Yu J, He X, Yi H and He X 2022 Multispectral differential reconstruction strategy for bioluminescence tomography *Front. Oncol.* **12** 768137

Mclennan G, Kumar D, Liu Y, Cong W, Hoffman E, McCray P, Wang L, Zabner J and Wang G 2005 Practical reconstruction method for bioluminescence tomography *Opt. Express* **13** 6756–71

Olsson C, Carlsson M, Andersson F and Larsson V 2017 Non-convex rank/sparsity regularization and local minima *Proc. IEEE Int. Conf. Comput. Vis.* (IEEE)

Parvitte B, Risser C, Vallon R and Zeninari V 2013 Quantitative simulation of photoacoustic signals using finite element modelling software *Appl. Phys. B* **111** 383–9

Phan D, Le H and Thi H 2018 Accelerated difference of convex functions algorithm and its application to sparse binary logistic regression *37th Int. Joint Conf. Artificial Intelligence* pp {IJCAI–18}

Qin C, Zhong J, Hu Z, Yang X and Tian J 2012 Recent advances in Cerenkov luminescence and tomography imaging *IEEE J. Sel. Top. Quantum Electron.* **18** 1084–93

Ren N, Liang J, Qu X, Li J, Lu B and Tian J 2010 GPU-based Monte Carlo simulation for light propagation in complex heterogeneous tissues *Opt. Express* **18** 6811

Ren S, Wang L, Zeng Q, Chen D, Chen 1 and Liang J 2020 Effective reconstruction of bioluminescence tomography based on GPU-accelerated inverse Monte Carlo method *AIP Adv.* **10** 105329

Rezaeifar B, Wolfs C J A, Lieuwes N G, Biemans R, Reniers B, Dubois L J and Verhaegen F 2023 A deep-learning assisted bioluminescence tomography method to enable radiation targeting in rat glioblastoma *Phys. Med. Biol.* **68** 155013

Selesnick I 2017 Sparse regularization via convex analysis *IEEE Trans. Signal Process.* **65** 4481–94

Su L, Chen L, Tang W, Gao H, Chen Y, Gao C, Yi H and Cao X 2024 Dictionary learning method based on k-sparse approximation and orthogonal procrustes analysis for reconstruction in bioluminescence tomography *J. Biophotonics* **17** e202400308

Tan B, Li Y, Zhao H, Li X and Ding S 2020 A novel dictionary learning method for sparse representation with nonconvex regularizations *Neurocomputing* **417** 128–41

Wang J and Shim B 2012 On the recovery limit of sparse signals using orthogonal matching pursuit *IEEE Trans. Signal Process.* **60** 4973–6

Wang S, Selesnick I W, Cai G, Feng Y, Sui X and Chen X 2018 Nonconvex sparse regularization and convex optimization for bearing fault diagnosis *IEEE Trans. Industrial Electronics* p 1

Wen F, Chu L, Liu P and Qiu R C 2018 A survey on nonconvex regularization-based sparse and low-rank recovery in signal processing, statistics, and machine learning *IEEE Access* **6** 69883–906

Yang D, Wang L, Chen D, Yan C, He X, Liang J and Chen X 2018 Filtered maximum likelihood expectation maximization based global reconstruction for bioluminescence tomography *Med. Biol. Eng. Comput.* **56** 2067–81

Yang W *et al* 2012 Comparison of Cerenkov luminescence imaging (CLI) and gamma camera imaging for visualization of let-7 expression in lung adenocarcinoma A549 cells *Nucl. Med. Biol.* **39** 948–53

Zhang C H 2010 Nearly unbiased variable selection under minimax concave penalty *Ann. Stat.* **38** 894–942

Zhang G, Zhang J, Chen Y, Du M, Li K, Su L, Yi H, Zhao F and Cao X 2024 Logarithmic total variation regularization via preconditioned conjugate gradient method for sparse reconstruction of bioluminescence tomography *Comput. Methods Programs Biomed.* **243** 107863

Zhang H, He X, Yu J, He X, Guo H and Hou Y 2021 L1-L2 norm regularization via forward-backward splitting for fluorescence molecular tomography *Biomed. Opt. Express* **12** 7807–25

Zhang Q *et al* 2011 Source sparsity based primal-dual interior-point method for three-dimensional bioluminescence tomography *Opt. Commun.* **284** 5871–6

Zhang X, Tian J, Qu Y, Wang J, Zahng M, Hu Z and Liu M 2017 In vivo 3D imensional radiopharmaceutical-excited fluorescence tomography *J. Nucl. Med.* **58** 169–74